Experimental study of a 3D printed geogrid embedded with FBG sensor for reinforcement of subgrade with underlying karst cave

Mengxi Zhang[1*], Hao Zhu[2], Jie Yang[3], Chengchun Qiu[4], Akbar A Javadi[5]

[1]Professor, Department of Civil Engineering, Shanghai University, Shanghai, 200072, China. Email: mxzhang@i.shu.edu.cn.

[2]PhD, Department of Civil Engineering, Shanghai University, Shanghai, 200072, China. Email: zhuhao2747@shu.edu.cn.

[3]MSc, Department of Civil Engineering, Shanghai University, Shanghai, 200072, China. Email: ay961113@163.com.

[4]Associate professor, Yancheng Institute of Technology, School of Civil Engineering, Yancheng 224051, China. Email: craigqiu@163.com.

[5]Professor, Department of Engineering, University of Exeter, Exeter, Devon EX4 4QF, UK. E-mail: A.A.Javadi@exeter.ac.uk.

Abstract: Road construction in karst areas is a challenging task. Combining the advantages of geosynthetics and fiber Bragg grating (FBG), this paper creatively presents a new type of FBG-3D printed geogrid, which allows reinforcement and accurate deformation monitoring. A series of model tests were carried out to investigate the mechanical and deformation characteristics of the subgrade with underlying karst cave reinforced by FBG-3D printed geogrid. The experimental results indicate that the fully coordinated deformation between FBG sensor and geogrid is successfully achieved by 3D printing technology, and the relationship between fiber wavelength and strain is obtained. The existence of cave has an adverse effect on the subgrade, but the FBG-3D printed geogrids effectively improve the bearing capacity and footing settlement, and the reinforcement effect increases with the decrease of geogrid spacing. In the cyclic loading experiments, the earth pressure inside the subgrade reinforced by geogrid changes as a half-sine wave in each cycle. The FBG sensors accurately measure the strain change inside the subgrade, and the data show that the deformation of measuring point above the cave model is the largest. The research conclusions provide important basic data for the construction and monitoring of highway and geotechnical engineering projects.

Keywords: fiber Bragg grating, geogrid, model test, underlying karst cave, cyclic loading

1. Introduction

Karst is a special landform caused by the long-term influence of groundwater on soil or soluble rocks. In addition to the cavities and funnels formed in the rock mass posing a serious threat to the stability of traffic tunnels, the karst caves developed in the overlying soil layer also cause a higher probability of collapse for the highway traffic (Alija et al., 2013; Qian and Lin, 2016; Lyn et al., 2020). China is one of the countries with the most extensive karst disasters in the world. The disaster-affected areas in China occupy one third of the land area, exceeding 3.5 million square kilometers (Zhao et al., 2018; Lai et al., 2020; Zheng et al., 2021). The spatial complexity and uncertainty of karst areas bring great risks to engineering construction. Therefore, a large number of highway projects passing through karst areas face the problem of karst collapse caused by karst caves inside the subgrade.

The low bearing capacity of the subgrade with underlying karst cave seriously affects its stability. When there are karst caves in the subgrade, natural conditions, groundwater or traffic loads will cause collapse, resulting in road cracking and subsidence. Therefore, it is necessary to carry out reasonable reinforcement according to the actual engineering situation. Grouting and backfilling are the main treatment techniques for karst caves with shallow depths. For deep karst caves, beam-slab spanning and roof reinforcement are generally used. However, these traditional reinforcement methods have long construction periods and adversely affect the environment. In recent years, the rapid development of geosynthetic reinforcement technology has provided new ideas for engineering construction and has been proved to significantly improve the mechanical properties of soils in engineering practices (Chawla et al., 2019; Xu et al., 2019; Dhanya et al., 2019; Sadeghi et al., 2020).

Geogrid is one type of geosynthetic that has been successfully used for stabilization of roads over weak subgrade (Shankar and Suresha, 2011). Its excellent applicability to subgrade reinforcement is mainly reflected in the improvement of subgrade bearing capacity and the control of uneven settlement. With regard to previous research, Baadiga et al. (2021) conducted a series of large-scale laboratory tests on road sections to evaluate the performance of geogrid reinforced base under various subgrade conditions and found that the optimum depth of geogrid in the base was one-third of the surface. Farsakh et al. (2016) carried out plate load test on a road section paved with geogrid on soft subgrade and reported improved deformation characteristics and bearing capacity. Bonaparte and Berg (1987) laid the geogrid horizontally under the base to reinforce the subgrade with underlying karst cave, and the results showed that the geogrid effectively prevented the sudden collapse of the pavement. The tensile property of geogrid can effectively reduce the differential settlement and lateral deformation of subgrade. Therefore, it has obvious advantages in preventing sudden damage caused by karst cave subsidence. However, because of the complex geological conditions in karst areas, the causes of formation, degrees of development and evolution rules of underground caves are quite different. These uncertainties will still bring security risks to the reinforced roads. Therefore, appropriate monitoring work must be carried out to keep abreast of the development of karst cave and the deformation of the overlying soil layer.

In recent years, the large-scale monitoring of karst geology has been mainly based on spatial conditions, such as geo-radar monitoring and time-domain reflectometry. These techniques are expensive and difficult to achieve continuous deformation monitoring. However, for underground structures reinforced by geosynthetics, deformation monitoring of the materials helps to reflect the mechanics, deformation characteristics of soil and structural stability. Most traditional measurement methods involve the use of strain gauges and vibrating wire strain sensors. But in practical engineering applications, the monitoring signal is easily influenced by external environmental factors (Liu et al., 2017). Also, they cannot achieve the complete coordinated deformation between the measured component and the instrument, which results in low accuracy and poor anti-interference ability. In recent years, Fiber Bragg Grating (FBG) has been widely used in many civil engineering applications to sense strains and deformations (Moyo et al., 2005; Barrias et al., 2019; Kou et al., 2019; Buckley et al., 2020; Pei et al., 2020; Song et al., 2021). As a typical optical-fiber-based sensing technique, the distinguishing features of FBG are low cost, good stability and almost absolute measurement, especially in geotechnical engineering (Bhaskar et al., 2021). For instance, You et al. (2019) proposed a soil strain measurement method based on FBG sensing technology and successfully obtained real-time soil strain data. Yoshida et al. (2002) used fiber Bragg grating arrays to conduct experiments and developed a slope deformation monitoring system. Xu et al. (2017) proposed a distributed optical fiber sensor to measure karst collapse strains. They conducted experiments involving long-term monitoring that could provide time series data on distribution of collapse-induced strains. Despite the clear advantages of FBG sensors, they also have some limitations. For example, attaching bare fiber to the instrument surface is easy and it can be readily replaced, but the sensor has poor fatigue performance and can be easily damaged. Therefore, FBG sensors are often protected in embedded applications.

In this study, FBG sensors are embedded into geogrid by 3D printing technology.

In this way, a new FBG-3D printed geogrid is designed, combining the advantages of both. In the design of FBG-3D printed geogrid, the following compatibility principles of materials are considered:

(1) Strength. The strengths of FBG sensor and geogrid should not affect each other as much as possible.

(2) Interface. The material of geogrid should be compatible with FBG sensor, to reduce the loss of deformation parameters.

(3) Size. When the geogrid is deformed due to external conditions, the FBG sensor should be consistent with its deformation.

(4) Field distribution. The field distribution environment of geogrid (such as stress-strain field, temperature field, etc.) should not be affected by FBG sensor materials.

In this way, geogrid, as a packaging structure, can not only protect FBG, but also self-sense the strain accurately.

At present, the related research on geosynthetics reinforcement is behind the needs of engineering practice in karst areas. Although some research on the stability of geosynthetic-reinforced soil above caves has been carried out (Wang et al., 1996), there are very few results on reinforcement methods with FBG sensors. In particular, cyclic loading has a significant impact on the bearing capacity and deformation of the subgrade with underlying karst cave, and a more accurate monitoring method is needed to analyze the behavior. Therefore, in this paper, an FBG-3D printed geogrid is developed and used to reinforce the subgrade with underlying karst cave by laboratory model experiments. According to the previous research on geosynthetics reinforcement, different factors (such as number of layers, length, spacing and arrangement position of materials) have certain influences on the results (Yoo, 2001). This study selects different geogrid layers and spacings as test conditions, aiming at analyzing the mechanical and deformation characteristics of the subgrade with underlying karst cave reinforced by FBG-3D printed geogrid under static and cyclic loading. The conclusions drawn from this study provide a basis for the development of new geosynthetic materials. The FBG-3D printed geogrid has huge potential for enriching construction techniques and monitoring methods in the fields of road and geotechnical engineering.

2. Materials and methods

2.1. Soil

A sand was used in this study as backfill materials, with uniformity coefficient (Cu) of 4.52 and curvature coefficient (Cc) of 0.20. Fig. 1 shows the particle size distribution curve of the sand tested by laser particle size analysis, which is then classified as poorly graded sand (SP) in accordance with ASTM D2487 2011. The physical properties of the sand are presented in Table 1.

In addition, the shear strength index has a direct influence on the bearing capacity of sand. Therefore, through triaxial tests on cylindrical samples with diameter of 38.1 mm and height of 76.2 mm under different confining pressures, the internal friction angle of the test sand was determined to be 35.7° when the relative density was 70%.

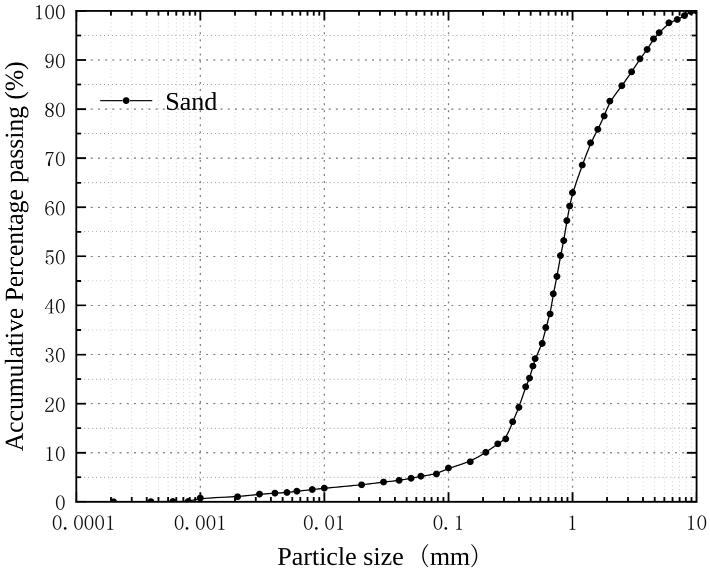

Fig. 1. Particle size distribution of test sand

Table 1 Physical properties of test sand

Properties	Value
Soil type	SP
D10 (mm)	0.21
D30 (mm)	0.52
D60 (mm)	0.95
Coefficient of uniformity (Cu)	4.52
Coefficient of curvature (Cc)	0.20
Specific gravity (Gs)	2.74
Maximum dry unit density (kN/m^3)	19.2
Minimum dry unit density (kN/m^3)	15.8

2.2. Fiber Bragg Grating (FBG) sensor

The FBG sensor is a monitoring element based on the sensitivity of optical devices to light, and the grating is written into the fiber core by the ultraviolet exposure method. An unpacked bare fiber consists of fiber core, cladding and protective layer (covering layer), as shown in Fig. 2. When the incident light is transmitted to the grating area through the optical fiber, the grating will only reflect the light signal centered at a specific wavelength, termed as the Bragg wavelength λ_B (Pei et al., 2017; Zheng et al., 2019). The related wavelength determination formula can be expressed as Eq. (1):

$$\lambda_B = 2n_{eff}\Lambda \quad (1)$$

where n_{eff} is the effective refractive index of the fiber core and Λ is the grating period.

Among many environmental variables, strain and temperature have a significant effect on FBG sensors. Strain and temperature change the Bragg wavelength through the periodic expansion or contraction of the grating (Luis et al., 2014; Xie et al., 2022). The corresponding wavelength shift $\Delta\lambda_B$ can be obtained as follows:

$$\frac{\Delta\lambda_B}{\lambda_B} = K_\varepsilon\varepsilon + K_T\Delta T \quad (2)$$

where ε is the axial strain of grating, ΔT is the temperature change of grating, and K_T and K_ε are the sensitivity coefficients of strain and temperature, respectively.

FBG sensors directly transmit optical signals through optical fibers instead of the electric signal transmission of ordinary sensors, so they have the advantages of low energy consumption and anti-electromagnetic interference. Furthermore, multiple measuring points can be accurately arranged to meet the measurement needs of key locations, so as to realize local series-distributed monitoring and continuous data acquisition. However, since the particularity of FBG sensor's optical fiber, it needs to be packaged and compatible with the tested component in consideration of strength, interface and size.

On the other hand, due to the data of center wavelength in grating areas obtained by demodulator cannot directly correspond to the strain parameters. The calibration experiment was carried out to determine the mathematical relationship between deformation and center wavelength (Fig. 3). One side of the optical fiber was naturally drooped until the wavelength data remained stable. Then, a 20g weight was loaded on the optical fiber coil every 25s for 4 times. After loading, the weights were removed one by one in the same way. In the whole process, it is necessary to strictly control the time of each step and avoid shaking.

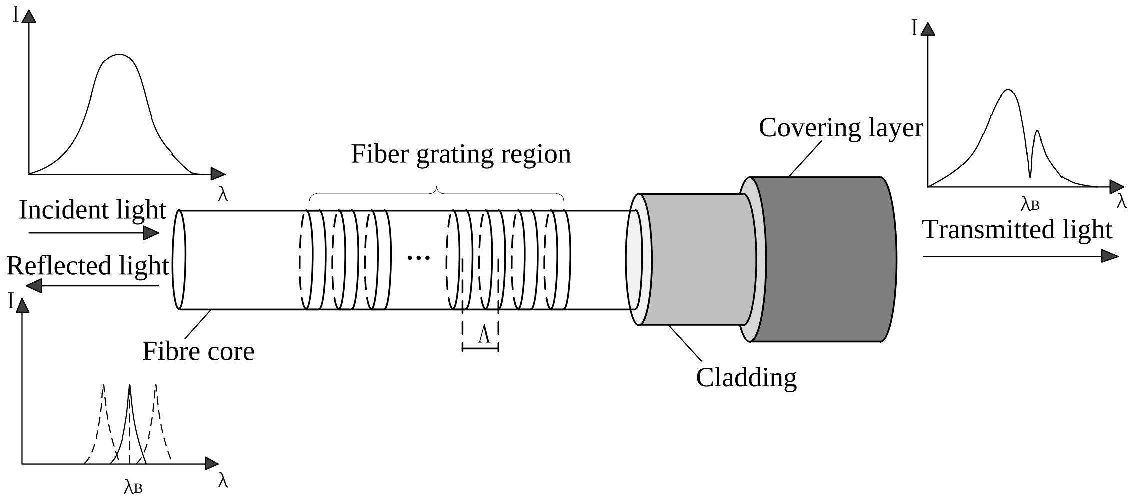

Fig. 2. Working principle of FBG sensors

Fig. 3. A view of FBG calibration experiment

2.3. FBG-3D printed geogrid

Combining FBG sensing technology and geosynthetic reinforcement, FBG sensor is embedded into the geogrid by 3D printing technology, developing an FBG-3D printed geogrid. In this way, geogrid is directly used as the packaging structure of FBG sensor so that we can ensure the complete coordinated deformation between the grating monitoring areas and geogrid, thus avoiding excessive loss of strain. The actual manufacturing process can be divided into three parts: geogrid model building, geogrid printing and FBG sensor embedding, and fiber packaging outside the geogrid. Fig. 4 shows the size of 3D printed geogrid and specific locations of optical fiber and grating. The mesh shape was square, with an aperture size of 10 mm×10 mm, and the strip width and thickness were 4 mm and 1.4 mm, respectively. The vibration caused by cyclic loading leads to continuous collision between geogrid and model box, which will affect the measurement accuracy of FBG sensor. Therefore, the FBG-3D printed geogrid has no direct contact with the side walls of the model box.

Carbon fiber was used as 3D printing material, with good compatibility, tensile strength and ductility. Through repeated tests, a layered printing thickness of 0.1mm and printing speed of 60 $mm \cdot s^{-1}$ were selected. When the printing progress reached 50%, the FBG sensor was placed in the designed position. At the same time, in order to prevent the optical fiber from shifting caused by the movement of printer nozzle, it was necessary to fix the optical fibers at both ends of the geogrid with sellotape. After 3D printing, the optical fiber outside the geogrid was protected by a PVC sleeve with a diameter of 2 mm and connected to the FBG demodulator. A tensile-strength test, as per

ASTM D6637 2015, was carried out on the specimen. Fig. 5 shows the relationships between tensile stress and strain of FBG-3D printed geogrid and 3D printed geogrid. Because their resistance to deformation mainly depends on the geogrid, their ultimate tensile strength is very close. However, at the initial stage of the test, for the same strain, the tensile stress of FBG-3D printed geogrid was slightly higher because the grating fiber was stretched. Table 2 describes the physical and mechanical properties of the FBG-3D printed geogrid.

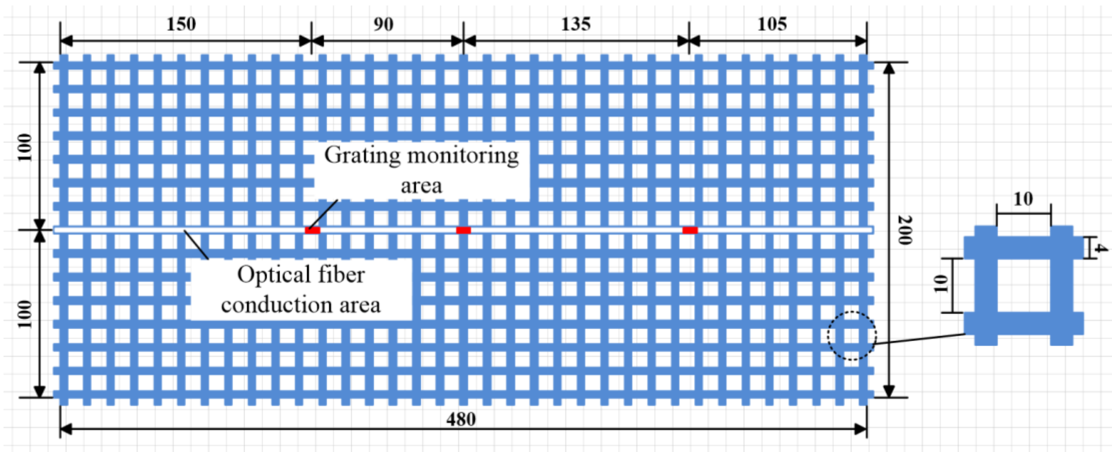

Fig. 4. Schematic diagram of FBG-3D printed geogrid (dimensions in mm)

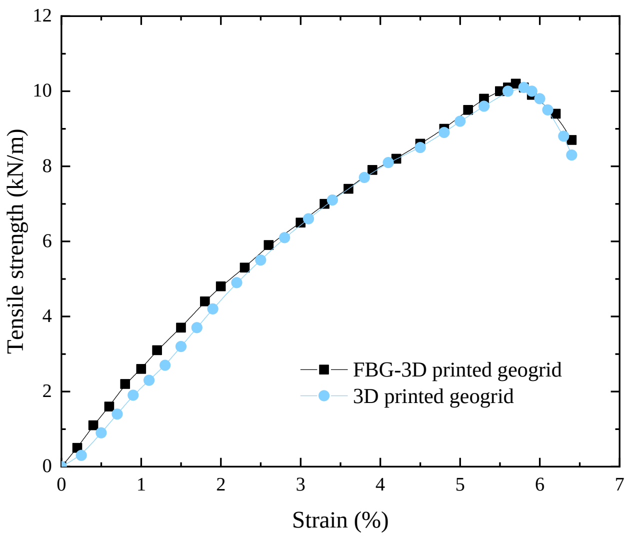

Fig. 5. Tensile stress-strain curves of 3D printed geogrid and FBG-3D printed geogrid

Table 2 Properties of FBG-3D printed geogrid

Parameter	Value
Aperture size (mm)	10×10
Thickness (mm)	1.4
Tensile strength at 2% strain (kN/m)	3.7
Tensile modulus at 2% strain (kN/m)	185
Ultimate tensile strength (kN/m)	10.2

2.4. Principles of similitude

The focus of this research is the analysis of deformation and reinforcement of a subgrade with underlying karst cave. To investigate the factors that influence the structure, scale model tests have been widely used in related research (He et al., 2021; Xu et al., 2021). Through similarity theory and dimensional analysis, the relationship between mechanical behavior of the scale model and the prototype structure can be quantitatively described. Considering the combination with the loading device and its stability during experiment, a model box is selected as the container for subgrade construction. The model box has internal dimensions of 600 mm × 290 mm × 300 mm (length × width × height) and is welded into a skeleton from a 25 mm thick steel plate. A high-strength toughened glass of 25 mm thickness is embedded in the box as a sidewall. Michalowski and Shi (2003) conducted a plate load test and found that the scale effect would be insignificant once the width and height of model are greater than 10 and 6 times the width of the footing. The width of the footing in this study is 50 mm, so the scale effects can be considered insignificant.

The similarity ratio is related to the engineering prototype and test model.

According to the similitude theory, the similitude coefficients, C_i, defined as the ratios of the prototype parameters i_p to the model parameters i_m, i.e.,

$$C_i = \frac{i_p}{i_m} \tag{3}$$

must be constant. Considering the dimensions of the model test, the geometric similarity scale is determined to be C_L=20. The similarity ratio of bulk-density is C_γ=1, and the similarity parameters are deduced as shown in Table 3.

Table 3 Similarity ratio of physical parameters

Parameters	Definition	Relations	Similarity ratio
Stress	$C_\sigma = \sigma_p/\sigma_m$	$C_\sigma = C_\gamma C_L$	20
Strain	$C_\varepsilon = \varepsilon_p/\varepsilon_m$	$C_\varepsilon = C_\mu$	1
Cohesion	$C_c = C_p/C_m$	$C_c = C_\sigma$	20
Density	$C_\gamma = \gamma_p/\gamma_m$	$C_\gamma = C_\sigma/C_L$	1
Elasticity modulus	$C_E = E_p/E_m$	$C_E = C_\sigma/C_\varepsilon$	20
Poisson's ratio	$C_\mu = \mu_p/\mu_m$	$C_\mu = C_\varepsilon$	1
Friction coefficient	$C_\varphi = \varphi_p/\varphi_m$	$C_\varphi = C_\mu$	1

C represents the similarity scale. Subscript, p represents the prototype, m represents the prototype model, σ represents stress, ε represents strain, c represents cohesion, γ represents bulk density, E represents modulus of elasticity, μ represents Poisson's ratio, φ represents angle of internal friction.

2.5. Analogue materials

In the mechanical model test, analogue materials should be selected according to the research object and conform to the relevant similarity principle (Li et al., 2021). Karst cave is usually an underground cave with a certain thickness formed by the erosion of surface water or the undercurrent of groundwater. During this process, the surrounding soil will disintegrate and finally be fixed into a random shape, with low strength and easy destruction. The failure mechanism of karst cave simulated in this test is shown in Fig. 6, including the following four stages.

(1) Karst cave is formed by the subsurface erosion of groundwater from soluble rock layers.

(2) With the development of the karst cave, the disintegrated soil is accumulated at the bottom of the cave due to gravity and isolated from groundwater. The side wall of the cave has a certain strength and maintains balance with the upper soil.

(3) External factors destroy the balance, and loose soil quickly collapses and accumulates in the cave due to karst collapse.

(4) The surrounding soil further collapses or slips to the center until it reaches a stable state.

It is assumed that karst cave is developed in the soil layer, and the influence of water is not considered. According to previous studies, similar materials simulating soft surrounding rock have high density, low strength and low elastic modulus (Xu et al., 2021), and materials that simulate karst caves have some similar characteristics with them. Considering uniformity of cross section and isotropy of materials, the cave model was made from gypsum powder by changing water content. Fig. 7 shows the cross section and dimensions of the cave model, with an outer diameter of 45 mm and a thickness of 2 mm. After iterative proportional adjustment, the mass ratio of water to gypsum powder which meets the requirements was determined as 1:1.4. The compressive strength of gypsum pipe obtained by uniaxial compressive test is 0.13 MPa.

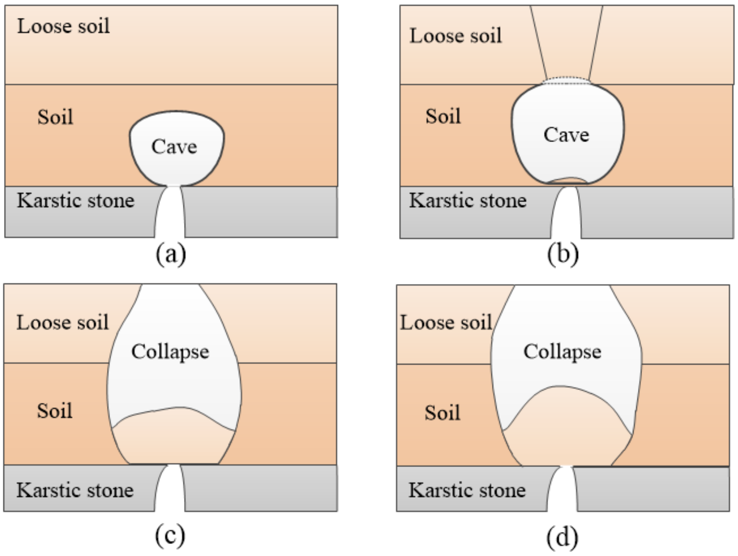

Fig. 6. Failure mechanism of a karst cave

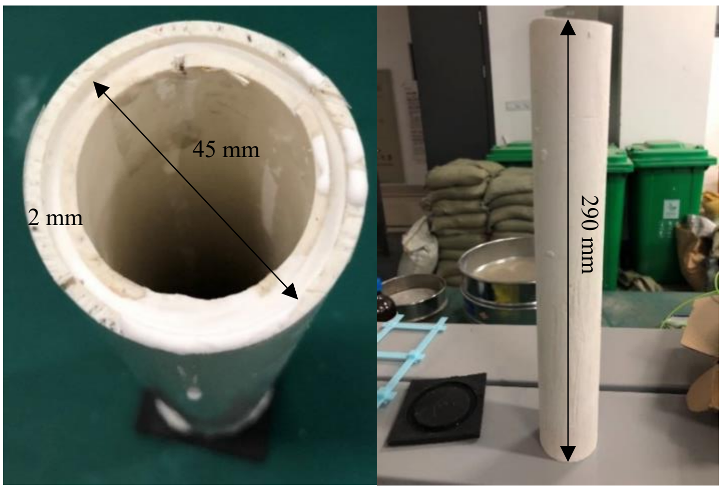

Fig. 7. Schematic diagram of cave model

2.6. Model test schemes

In order to carry out the subgrade model test in laboratory scale, the loading chamber located in dynamic triaxial laboratory of Department of Civil Engineering, Shanghai University was used. The design of the test is based on a subgrade with a width of 12 m and a height of 6 m, having a circular karst cave. The stability of karst caves is closely related to their location and size. Hubbard and Balfour (1993) investigated the engineering concerns of a proposed highway construction in karst area and found that the cave passage broke within 5m below the subgrade, which was a potential safety hazard. Zhao et al. (2021) analyzed the stability of karst cave in the soil layer through the limit theorem and found that gravity could induce damage to a cave with a critical radius of 1.25 m, but additional load conditions would reduce this critical radius. Considering the influence of traffic load on subgrade, the test design assumes that there is a circular cave with a diameter of 0.9 m in the soil layer at a depth of 4.1 m below subgrade.

The different experimental designs considered are shown in Table 4. Five groups of tests were carried out independently, with a non-reinforced scenario being set as control sample. The influence of number of geogrid layers on reinforcement effect was studied between test conditions B and C. Furthermore, the effect of spacing of geogrids was considered under test conditions C1, C2, C3. The model test scheme is shown in Fig. 8. Regarding the layout of geogrids, Yetimoglu et al. (1994) found that the improvement of bearing capacity will be greatly reduced when the depth of single-layer geogrid exceeds 1.2 B, where B is the width of footing. The footing width of this test is 50 mm, so the arranged depth of single-layer geogrid is 60 mm. On the other hand, Latha and Somwanshi (2009) arranged geogrid at depths of 2 B and 2.67 B to study the reinforcement effect of multi-layer geogrids. Therefore, in this test, the spacing of double-layer geogrids is 50 mm and 70 mm. An additional test condition of 90 mm is added to obtain the strain data of the soil close to the cave, which is helpful in analyzing the deformation near the cave.

Before preparation of the test model, low friction silicone grease was used to minimize possible friction between the walls of the test box and the assembled soils. In the process of filling soil into the model test box, each layer was compacted to the relative density of 0.8 from bottom to top. When the thickness of filling soil reached the target height, the corresponding cave model, soil pressure cells and FBG-3D printed geogrids were laid at preset places. The relevant test steps are shown in Fig. 9. In the experiments, the dynamic and static apparatus slightly modified in loading method (USTX-2000 of GCTS, USA), was used for loading, and the loading element was fixed on the upper part of the reformed model box by two columns. The data acquisition device consisted of optical fiber wavelength modulator, and soil pressure and displacement data acquisition. In the static loading test, a load was applied on the middle of the subgrade surface, and the loading speed was set as 3 N/s. The test stopped when the displacement suddenly changed and the subgrade suffered from overall shear failure. However, the research on cyclic loading is more in line with the actual situation of instantaneous and multi-frequency traffic load on subgrade. The subgrade with underlying karst cave has greater risk of damage under cyclic loading. Geosynthetics reinforcement technology can effectively improve the stability of subgrade and reduce the settlement, but the slight deformation of soil inside subgrade under cyclic loading is generally difficult to obtain. Therefore, FBG-3D printed geogrid was used to reinforce the subgrade and collect real-time and continuous data at the designated key positions.

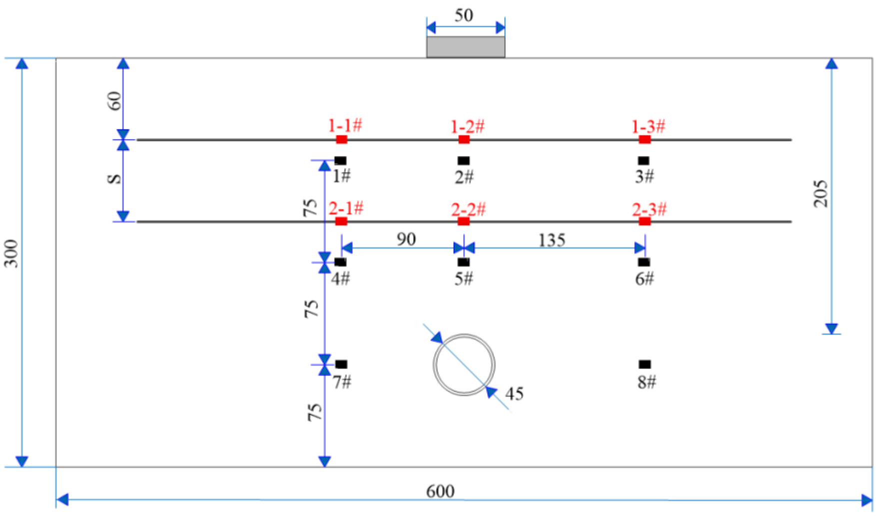

Fig. 8. A schematic view of the reinforced subgrade with an underlying cave (dimensions in mm)

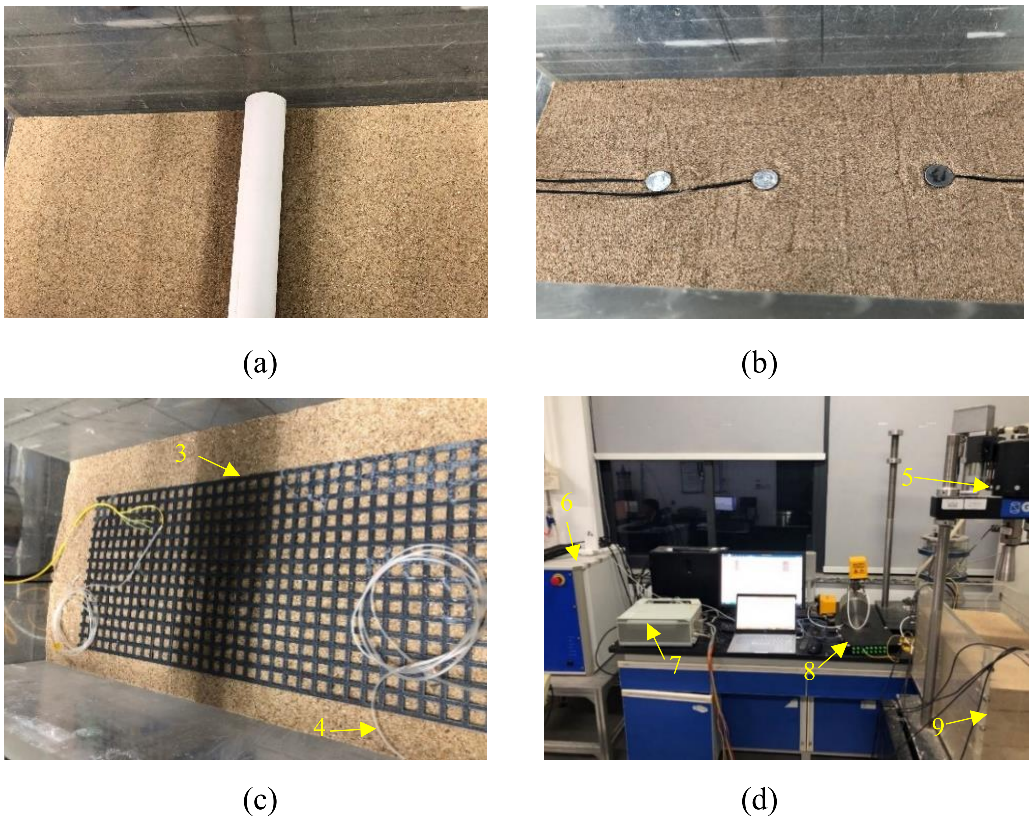

Fig. 9. The general procedure of model test. (a) Placing earth cave model; (b) Embedding earth pressure sensors; (c) Placing FBG-3D printed geogrids; (d) Overview of model test system. 1. Earth cave model; 2. Soil pressure sensor; 3. 3D printed geogrid; 4. FBG; 5. Loading system; 6. Data acquisition instrument; 7. Soil pressure dynamic collection box; 8. Optical fiber wavelength modulator; 9. Model test box

Table 4 Different test conditions of model test

Test Conditions	Reinforced Layer	Geogrids Spacing /mm
A	/	/
B	1	/
C1	2	50
C2	2	70
C3	2	90

2.7. Cyclic loading waveform

Traffic loading is an instantaneous load related to vehicle structure, vehicle speed, road performance, etc. (Chai et al., 2002). Huang et al. (1993) reported that when a wheel load is at a considerable distance from a given point in the pavement, the stress at that point is zero and when the load becomes directly above the point considered, the stress at that point is maximum. Therefore, it is reasonable to assume the traffic loading to be a half-sine or triangular loading (Razouki et al., 2011). In this test, the traffic load on the subgrade surface is simulated by a stable half-sine wave (Fig. 10) as:

$$F(t) = P \sin^2 \frac{\pi t}{d} \tag{4}$$

where P is the load amplitude, t is the time, and d is the period of cyclic load.

Liu et al. (2023) demonstrated that the influence of traffic load on subgrade can be accurately simulated when the frequency of cyclic load is 1 Hz. After multiple parallel tests, 57% of the ultimate bearing capacity of unreinforced subgrade with underlying karst cave under static loading, i.e., 27.6 kPa, was taken as the loading amplitude of cyclic loading. The frequency of cyclic loading was 1 Hz. Taking the subgrade strengthened by single-layer geogrid as an example (Test condition B), Fig. 11 shows the relationship between footing displacement and number of cycles. When the load is applied for the first time, the footing displacement of the subgrade increases sharply, and it tends to be stable after several cycles. During this process, the sand is repeatedly compressed under cyclic load to improve the contact between soil particles and geogrid meshes, thus strengthening the interlocking effect. In each loading cycle, with the application of half-sine cyclic load, the footing displacement of subgrade also changes in a half-sine wave.

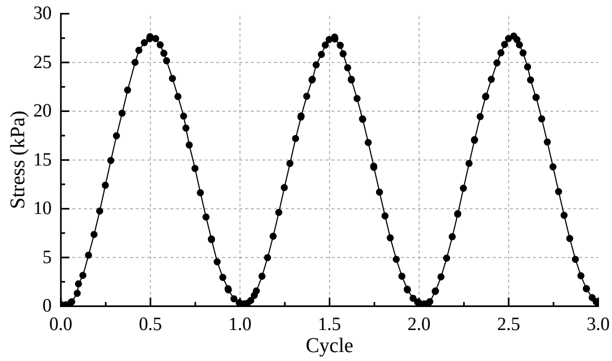

Fig. 10. Waveform of cyclic load

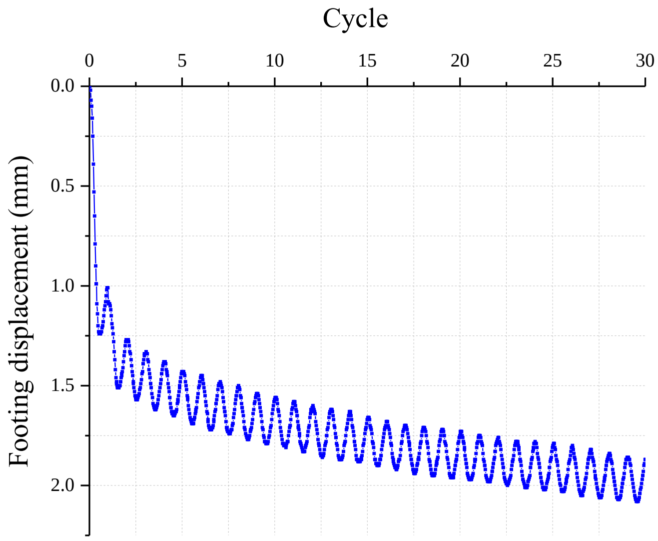

Fig. 11. Relationship between footing displacement and number of cycles for subgrade strengthened by a single-layer geogrid

3. Results and discussions

3.1. Calibration test

In order to obtain the relationship between deformation and central wavelength of FBG, a calibration experiment was carried out. The stable wavelength variation of FBG is particularly important in this study. As shown in Fig. 12, under the action of constant force, the wavelength of FBG is unchanged. However, the wavelength of FBG is very sensitive to the changes in the force. The strain can be obtained by the action of force, which can be expressed as equation (5):

$$\varepsilon = \frac{F}{EA} \tag{5}$$

where *F* is the force on the optical fiber, *E* is the elastic modulus of the optical fiber, which is 62.5 GPa, and *A* is the cross-sectional area of the optical fiber, which is 8.767

$\times 10^{-8}$ m^2.

A corresponding relationship can be obtained by fitting the variation of wavelength and strain data under different forces, as shown in Fig. 13. The best fit mathematical relationship between the strain and the variation of wavelength is obtained as:

$$\varepsilon = 21.42941\frac{\Delta\lambda}{\lambda} - 0.00007 \qquad (6)$$

where ε is the strain of FBG, $\Delta\lambda$ is the amount of change in wavelength, λ is the value of wavelength. The coefficient of determination R^2 for this relationship is about 0.96, which shows a very good fit. The results show that the FBG sensors embedded in 3D printed geogrid have good performance. Under the action of force, the measurement accuracy and sensitivity are very high, which meets the requirements of this experiment for strain measurement inside subgrade.

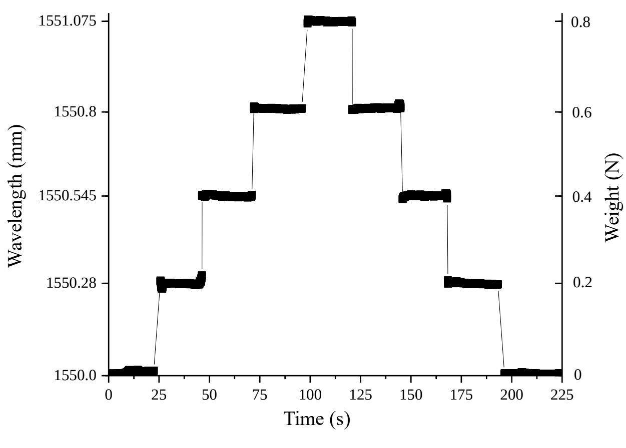

Fig. 12. Variation of FBG wavelength with weight and time

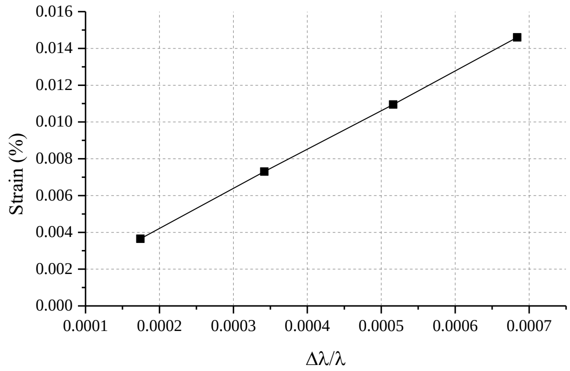

Fig. 13. The relationship between strain and central wavelength

3.2. Static loading test of subgrade

3.2.1 Ultimate bearing capacity

Fig. 14 shows the relationship between the bearing pressure and displacement of subgrade under static loading. In general, the bearing pressure of the subgrade in all test conditions increases linearly in a certain proportion with the increase of the footing displacement. When the footing displacement of the subgrade suddenly changes, it is considered that the embankment has reached the critical failure point, and the ultimate bearing capacity of subgrade has been achieved. For unreinforced subgrade, the ultimate bearing capacity is 82.14 kPa without karst cave (preliminary test). However, the existence of the underlying karst cave makes its ultimate bearing capacity only 48.38 kPa, which shows a reduction of 41.1% and poses a threat to subgrade. Therefore, it is necessary to reinforce the subgrade.

As shown in the results of test condition B, the ultimate bearing capacity of subgrade is increased to 64.7 kPa and the footing displacement at the time of failure is

1.94 mm after a single-layer geogrid reinforcement. This shows that the strength and stability of subgrade are significantly improved by geogrid reinforcement, and the reinforcement effect is more obvious with the increase of the number of geogrid layers. Similarly, the spacing between geogrids also has an influence on the reinforcement effect. In this study, the minimum spacing between the geogrids in the reinforced subgrade (S=50 mm) with underlying karst cave provides the highest ultimate bearing capacity of 87.27 kPa, which is 80% higher than that without reinforcement, and the footing displacement at failure is 1.5 mm. During the loading process, the sand is gradually compacted, resulting in a larger contact interface with geogrid. In this way, the friction and the interlocking effect between geogrid and sand reduce the stress concentration effect of subgrade, resulting in greater shear strength. Although karst caves destroy the integrity of subgrade and create obvious weak points, but as expected, the stability of subgrade after geogrid reinforcement is significantly improved.

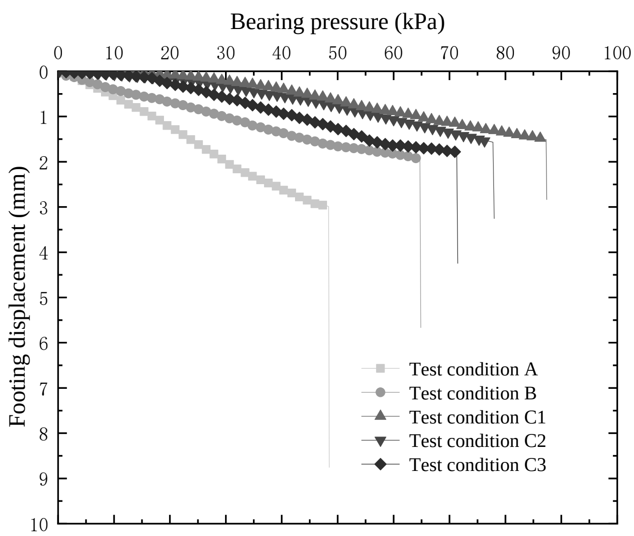

Fig. 14. The bearing pressure-displacement relationship curve of subgrade under different test conditions

3.2.2 Deformation

In order to analyze the internal deformation of the subgrade with underlying karst cave under different test conditions, FBG-3D printed geogrids are placed at specific positions, as shown in Fig. 8. After the calibration experiment, the performance of FBG in 3D printed geogrid can be evaluated. Therefore, not only the geogrid can play a role in strengthening the subgrade, but it also has the ability to detect deformation. Fig. 15 shows the curve for load-strain relations of subgrade reinforced by single-layer geogrid. Considering the above analysis of the ultimate bearing capacity of subgrade, the test condition C1 with best reinforcement effect (double-layer geogrid) is selected for comparison.

In the initial stage of loading, the strain of the geogrid increases slowly. However, with the continuous increase of loading, the strain of each measuring point rises rapidly following a nonlinear trend, especially near the footing. For the subgrade reinforced with single-layer geogrid, after the load exceeds 20 kPa, the geogrid begins to be stretched significantly, as shown in Fig. 15 (a). But this situation changes by increasing the number of layers of geogrid. At the same position (the first layer of geogrid), the maximum strain of each measuring point decreases significantly when the subgrade reinforced with double-layer geogrid. In addition, it can be noticed that for the geogrid in the second layer, the maximum strain of each monitoring point is less than 2000 $\mu\varepsilon$, and the load at which the strain begins to increase rapidly exceeds 50 kPa. In general, it is difficult to obtain the deformation of soil inside subgrade, but this problem can be solved by connecting the deformation of geogrid with soil by FBG sensor. The soil particles in direct contact with the geogrid increase the friction of contact surface after loading, so that the geogrid can effectively exert its binding force on the soil while stretching. Moreover, increasing the number of geogrid layers not only reduces the stress concentration effect, but it also allows to obtain the soil deformation data in deeper areas.

The experimental results prove that the FBG technology can be applied to monitoring of subgrade, and the deformation of the specified positions can be obtained stably during the whole loading process. Especially when the subgrade has potential safety hazards such as the underlying karst cave, the real-time deformation monitoring can provide basic data for the design and maintenance of subgrade, which has important research and application value.

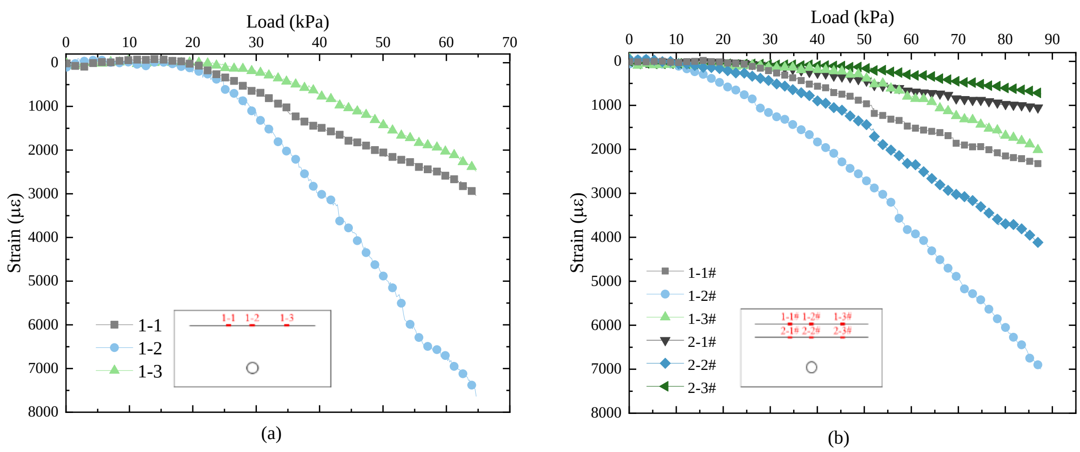

Fig. 15. Curve for strain-load relations of geogrid reinforced subgrade under different test conditions. (a) Test condition B; (b) Test condition C1

3.3. Cyclic loading test of subgrade

3.3.1 Accumulative settlement

To obtain the variation of vertical settlement of footing for the subgrade with underlying karst cave after multiple cycles, cyclic load tests were carried out under different test conditions. The performance of the subgrade under every cycle is presented in Fig. 11. In this section, considering the large number of cycles (15,000), the data are simplified and key points are displayed. Then the relationship between footing settlement and cycle of the subgrade is obtained, as shown in Fig. 16. It can be seen that in the initial stage of cyclic load application, the cumulative settlement of the subgrade with underlying karst cave increases rapidly under all test conditions. After that, with the number of cycles exceeding 1000, the growth rate of footing settlement of subgrade slows down. When the number of cycles reaches 15,000, the cumulative settlement of the unreinforced subgrade with underlying karst cave reaches 12.46 mm, resulting in a large deformation. However, this situation is significantly improved with the reinforcement of geogrid. For the subgrade with underlying karst cave reinforced with a single-layer geogrid, the cumulative settlement is reduced to 10.13mm, which is 18.7% lower than that without reinforcement. Fig. 17 shows the progressive deformation of the subgrade with underlying cave strengthened by a single-layer geogrid at different cycles. At the initial stage of cyclic loading, the displacement of the footing is small and the geogrid reinforcement layer acts as a rigid layer. As cycles increase, the soil beneath the footing moves downward making reinforcement layers to deform, leading to the soil uplift on both sides of the footing. This settlement-cycle variation is similar to the results of Fig. 16.

The footing settlement of subgrade is further reduced with the increase of the number of geogrid layers. By controlling the spacing between the geogrids, the footing settlements of the subgrade under test condition C are 7.36 mm (S=50 mm), 8.01 mm (S=70 mm) and 9.44 mm (S=90 mm), respectively, which are 40.93%, 35.71% and 24.2% lower than those without reinforcement. This shows that reducing the spacing is helpful to further exert the binding force of geogrid on sand. On the other hand, the sand with poor gradation will physically change its soil volume and porosity under the action of cyclic loading. During this process, the sliding and rolling of sand particles are closely related to the friction. Geogrid can interlock with sand particles to produce a more stable soil structure, thus improving the deformation inside subgrade. This remarkable reinforcement effect is more prominent after increasing the number of geogrid layers. Generally, under cyclic loading, the best scheme for strengthening the subgrade with underlying karst cave is the test condition C1, which is consistent with the result under static load.

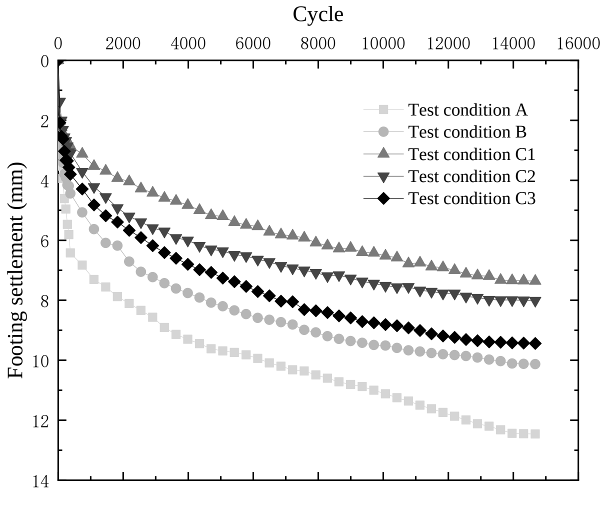

Fig. 16. Variations of footing settlement with number of cycles for subgrade under

different test conditions

(a) (b)

Fig. 17. Photographs showing the deformation of the subgrade with underlying cave strengthened by single-layer geogrid, (a) 2000 cycles; (b) 15000 cycles.

3.3.2 Earth pressure

For the subgrade with underlying karst cave, the analysis of internal earth pressure can effectively reveal the reinforcement mechanism, especially under cyclic loading. Therefore, the earth pressure sensors were arranged at the designated positions in horizontal and vertical directions, as shown in Fig. 8. Because the data of earth pressure inside subgrade during whole loading process are too large, the earth pressures of first 100 cycles are selected for analysis. For the subgrade under test condition C1 with the best reinforcement effect under static loading, Fig. 18 shows the variation of earth pressure during each cycle (position 2#). It can be seen that the earth pressure changes with the application of cyclic load and presents a half-sine waveform. After the applied load becomes stable, the earth pressure varies regularly between 13 kPa and 28 kPa, and its amplitude decreases with the increase of cycles. The distribution of earth pressure in different positions is analyzed, as shown in Fig. 19. In the vertical direction, since positions 2# and 5# are on the same line as the loading area, the value of earth pressure is larger. The earth pressure amplitude of the upper position 2# is 13.2 kPa, which is 1.5 times that of position 5#. However, there is an obvious difference of earth pressure in the horizontal direction. The earth pressure amplitudes of positions 4#, 5# and 6# are 1.2 kPa, 8.8 kPa and 0.3 kPa respectively from left to right. This shows that the earth pressure in the area above the cave is high, which leads to a greater risk of collapse. After the subgrade is reinforced with geogrids, the stress concentration effect is improved, and the internal earth pressure can be effectively borne by the geogrid reinforcement layer in the vertical direction. In addition, the excellent tensile performance of geogrid can play a significant role in the horizontal direction and reduce the stress diffusion. This kind of stable reinforcement under cyclic load is particularly important and meaningful.

In addition, the variation of the earth pressure above the karst cave (position 5#) under cyclic loading needs to be further analyzed. Fig. 20 shows the test results of subgrade with different geogrid layers and geogrid spacings. Among these influencing factors, the number of geogrid layers has a great influence on the earth pressure, as shown in Fig. 20(a). For the subgrade with underlying karst cave reinforced with double-layer geogrids (with a spacing of 70 mm), the peak earth pressure reaches 16.9 kPa, which is about twice that of the subgrade reinforced with single-layer geogrid. On this basis, the change of geogrid spacing will also affect the earth pressure. In general, the peak earth pressure decreases with the increase of geogrid spacing, as shown in Fig. 20(b). The earth pressure for all test cases exhibits a half-sine waveform at each cycle, and its peak value is 18.7 kPa at a minimum geogrid spacing of 50mm. It can be seen that reasonable arrangement of geogrid reinforcement layer can effectively control the stress transfer in soil. Especially under cyclic load, the earth pressure variation of subgrade can maintain a stable variation, which proves that geogrid reinforcement can improve the safety of the subgrade with underlying karst cave.

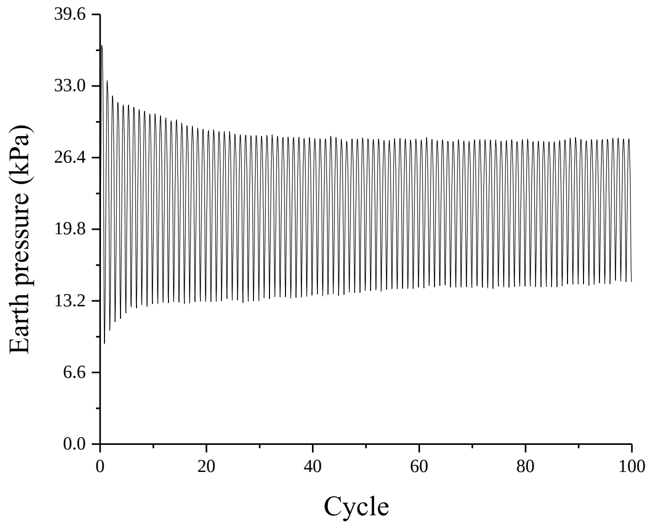

Fig. 18. The curve of earth pressure depending on cyclic load

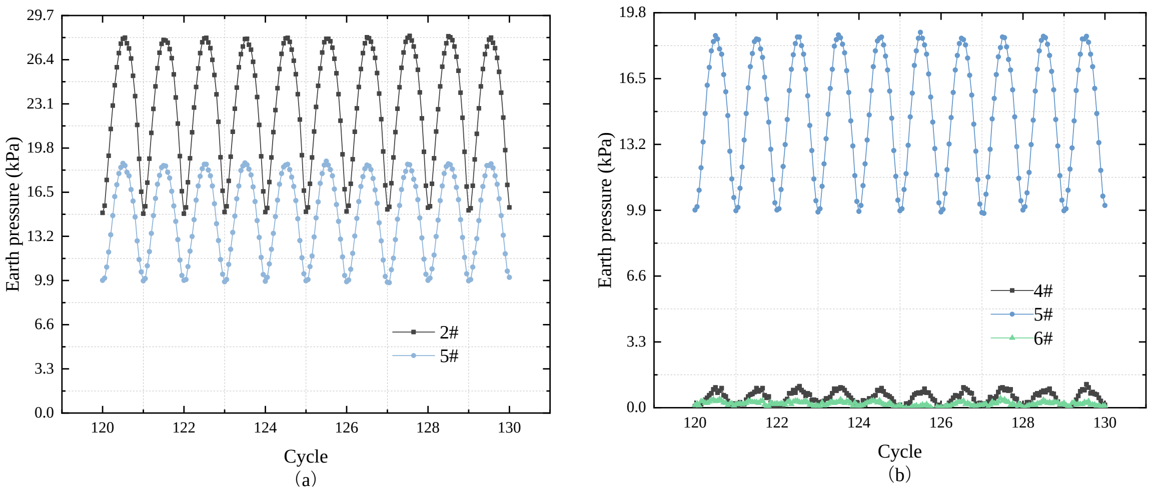

Fig. 19. The earth pressure-cycle curve of subgrade under test condition C1. (a) Vertical direction; (b) Horizontal direction

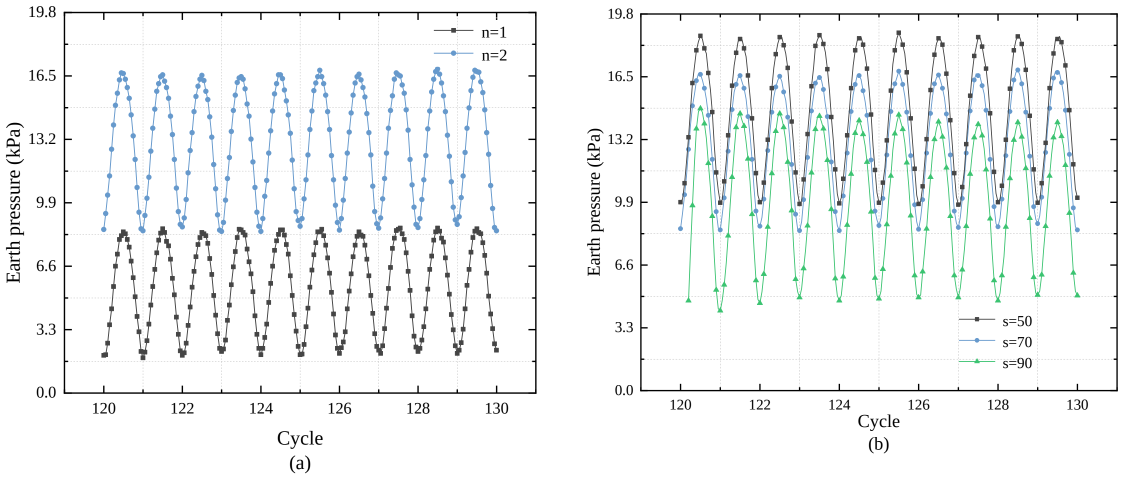

Fig. 20. The earth pressure- cycle curve of position 5# under different influencing factors. (a) Number of geogrid layers; (b) Spacing of geogrids

3.3.3 Deformation

Because of the vibration caused by cyclic loading, it is generally difficult to accurately obtain the deformation data of subgrade during the whole loading process. However, the FBG sensor combined with geogrid by 3D printing technology not only monitors the deformation of a specific location, but also plays a reinforcement role. Fig. 21 shows the wavelength variation curve of the middle measuring point (2-2#) under test condition C1, where the wavelength demodulator recorded the wavelength every 200ms. In this process, the sand becomes more and more compact and the wavelength presents a trend of reciprocating growth. The partial enlargement of Fig. 21 shows that the wavelength is approximately one cycle every five points, that is, one strain cycle per second. This is consistent with the frequency of cyclic loading, which also reflects the reliability of FBG sensor measurement data.

FBG monitoring is done in real-time, and the monitoring data is too huge.

Therefore, in order to facilitate the analysis, a monitoring data is taken every 80 points (every 40s). According to the formula in Section 3.1, the measured wavelength can be converted into strain data. The test results show that with the increase of number of cycles, the strain continues to increase. However, the strain of specific location is closely related to the reinforcement effect of geogrid. Fig. 22 shows that when a single-layer geogrid is used to reinforce the subgrade, the position 1-2#, which is closest to footing in horizontal direction, has the largest strain and exhibits irregular inflection during the loading process. But this situation is obviously improved with the increase of geogrid layers. As shown in Fig. 23, the deformation of double-layer geogrid is significantly reduced. In positions 1 and 2, the strain is 1260 με after 14,000 cycles, which is approximately 45% lower than that of single-layer geogrid reinforcement. In the vertical direction, the strain changes at positions 1-2# and 2-2# are relatively stable and reflect the waveform variation of the cyclic load to a certain extent. The existence of the karst cave makes the soil directly below the footing to be squeezed outward, and finally affects the deformation of the geogrid. At the beginning of the cyclic load, the displacement of the footing is small and the single-layer geogrid reinforcement layer acts as a rigid layer. However, with the increase of cycles, the deformation of the geogrid increases. Once the mobilized tensile force exceeds the ultimate tensile strength of geogrid, the fracture of reinforcement can be predicted. Therefore, it is necessary to increase the number of reinforcement layers, which makes the soil bear stronger dynamic characteristics. Although the deformation of geogrid cannot be completely equated with the deformation of subgrade, these strain data can provide necessary information to support the daily maintenance and monitoring of the road, and also have value for research and application.

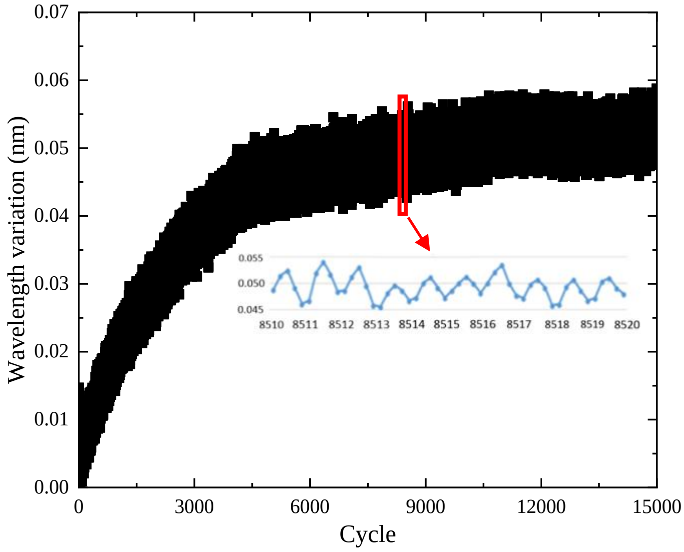

Fig. 21. Wavelength variation of 2-2# measuring point under test condition C1

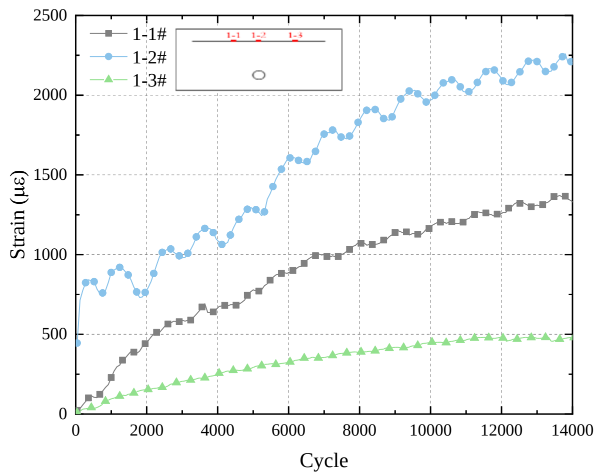

Fig. 22. Variation of strain of geogrid reinforced subgrade with loading cycles under test condition B

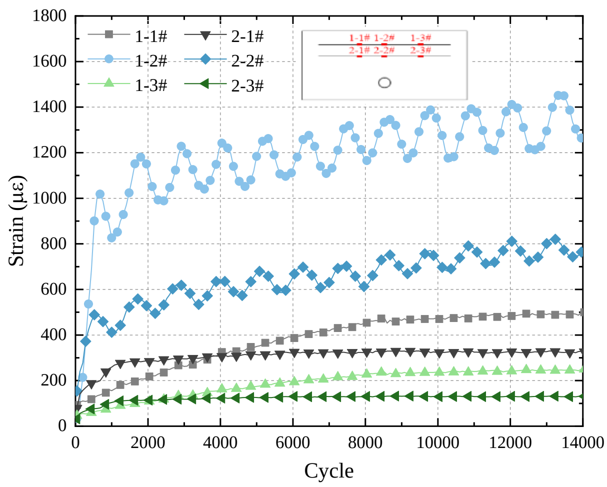

Fig. 23. Variation of strain of geogrid reinforced subgrade with loading cycles under test condition C1

4. Conclusions

In this paper, a self-sensing geogrid that can monitor strain in real time was developed and applied to the model test of a geogrid reinforced subgrade with an underlying karst cave. By controlling the number of geogrid layers and geogrid spacing, the deformation characteristics and mechanical properties of the subgrade under static and cyclic loads were analyzed and discussed. The conclusions of this research can be summarized as the following:

(1) The self-sensing geogrid designed by combining FBG sensor and 3D printing technology realizes the complete coordinated deformation between FBG sensor and geogrid. Through calibration experiment, the wavelength measured by FBG is effectively related to the strain of geogrid. This ensures that strain changes can be monitored in real time and accurately while the subgrade is reinforced by geogrid.

(2) The existence of underlying karst cave reduces the stability of the subgrade and poses a threat to the safety. Under static loading, geogrid reinforcement can effectively improve the ultimate bearing capacity of subgrade with underlying karst cave and obviously reduce the surface settlement when the subgrade is damaged. Compared with the unreinforced state, the ultimate bearing capacity of the subgrade reinforced with double-layer geogrids (S=50mm) is increased by 80%. The geogrid deforms the most in the direction in which the load is applied, and the deformation decreases as the number of geogrid layers increases.

(3) In the initial stage of cyclic loading, the cumulative settlement of the subgrade with underlying karst cave increases rapidly until the number of cycles reaches 1000, then the growth rate slows down. Compared with the unreinforced subgrade, the cumulative settlement of the reinforced subgrade can be reduced by 40.93% at the maximum. Under the same number of cycles, the cumulative settlement of reinforced subgrade with an underlying karst cave increases with the increase of the loading amplitude.

(4) During each cycle, the earth pressure inside the subgrade reinforced by geogrid changes in a half sine wave. Among the many influencing factors, the number of geogrid layers has a great influence on the earth pressure. The peak earth pressure of the subgrade reinforced by double geogrids (S= 70mm) reaches 16.9 kPa, which is about twice that of the subgrade

reinforced by single geogrids. Moreover, the earth pressure increases further with the decrease of geogrid spacing.

(5) Whether under static load or cyclic load, the deformation of geogrid decreases from the loading center to both sides. In the horizontal direction, the deformation of measuring point above the karst cave is the largest. In the vertical direction, the strain change below the loading point reflects the waveform of cyclic load to some extent.

Acknowledgement

The authors thank the Funding received from the National Natural Science Foundation of China under grant No. 51808481 and the Natural Science Foundation of Jiangsu Province under grant No. BK20170477.

References

ASTM D2487-11, 2011. Standard Practice for Classification of Soils for Engineering Purposes. West Conshohocken, PA, USA.

ASTM D6637, 2011. Standard Test Method for Determining Tensile Properties of Geogrids by the Single of Multi-Rib Tensile Method. ASTM International, West Conshohocken, PA, USA.

Abu-Farsakh, M.Y., Akond, I., Chen, Q.M., 2016. Evaluating the performance of geosynthetic- reinforced unpaved roads using plate load tests. Int. J. Pavement Eng. 17 (10), 901-912.

Alija, S., Torrijo, F.J., Quinta-Ferreira, M., 2013. Geological engineering problems associated with tunnel construction in karst rock masses: The case of Gavarres tunnel (Spain). Eng. Geol. 157, 103-111.

Baadiga, R., Saride, S., Balunaini, U., Madhira M.R., 2021. Influence of tensile strength of geogrid and subgrade modulus on layer coefficients of granular bases. Transp.

Geotech. 29, 100557.

Barrias, A., Casas, J.R., Villalba, S., 2019. Fatigue performance of distributed optical fiber sensors in reinforced concrete elements. Constr. Build. Mater. 218, 214-223.

Bhaskar, C.V.N., Pal, S., Pattnaik, P.K., 2021. Recent advancements in fiber Bragg gratings based temperature and strain measurement. Results in Optics 5, 100130.

Bonaparte, R., Berg, R.R., 1987. The use of geosynthetics to support roadways over sinkhole prone areas. In: Proceedings of the 2nd multidisciplinary conference on sinkholes and the environmental impacts of karst. Orlando, pp. 437-450.

Buckley, R.M., McAdam, R.A., Byrne, B.W., Doherty, J.P., Jardine, R.J., Kontoe, S., Randolph, M.F., 2020. Optimization of impact pile driving using optical fiber Bragg-Grating measurements. J. Geotech. Geoenviron. Eng. 146 (9), 04020082.

Chai, J.C., Miura, N., 2002. Traffic-load-induced permanent deformation of road on soft subsoil. J. Geotech. Geoenviron. Eng. 128 (11), 907-916.

Chawla, S., Shahu, J.T., Gupta, R.K., 2019. Design methodology for reinforced railway tracks based on threshold stress approach. Geosynth. Int. 26 (2), 111-120.

Dhanya, J.S., Boominathan, A., Yu, Y., Banerjee, S., 2019. Performance of geo-base isolation system with geogrid reinforcement. Int. J. Geomech. 19 (7), 04019073.

He, B.G., Zhang, Y., Zhang, Z.Q., Feng, X.T., et al., 2021. Model test on the behavior of tunnel linings under earth pressure conditions and external water pressure. Transp. Geotech. 26, 100457.

Hubbard, D.A., Balfour, W.M., 1993. An investigation of engineering and environmental concerns relating to proposed highway construction in a karst terrane. Environ. Geo. 22, 326–329.

Huang, Y.H., 1993. Pavement analysis and design. Prentice-Hall, Inc., Englewood Cliffs.

Kou, H.L., Yu, F., Liu, T., 2019. Strain monitoring on PHC pipe piles based on fiber Bragg grating sensors. J. Perform. Constr. Fac. 33 (2), 04019003.

Lai, J.X., Zhou, H., Wang, K., Qiu, J.L., Wang, L.X., Wang, J.B., 2020. Shield-driven induced ground surface and Ming Dynasty city wall settlement of Xi’an metro. Tunn. Undergr. Space Technol. 97, 103220.

Latha, G.M., Somwanshi, A., 2009. Bearing capacity of square footings on geosynthetic reinforced sand. Geotext. Geomembranes 27, 281–294.

Li, L.P. Shang, C.S. Chu, K.W. Zhou, Z.Q. et al., 2021. Large-scale geo-mechanical model tests for stability assessment of super-large cross-section tunnel. Tunn. Undergr. Space Technol. 109, 103756.

Liu, K.F., Feng, W.Q., Cai, Y.H., Xu, H., Wu, P.C., 2023. Physical model study of pile type effect on long-term settlement of geosynthetic-reinforced pile-supported embankment under traffic loading. Transp. Geotech. 38, 100923.

Liu, W.Q., Wang, B.S., Zhou, Z., Cao, D.D., Zhao, Y.Q., 2017. Design and testing of a large-scale shape-monitoring sensor based on Fiber-Bragg-Grating sensing technique for pavement structure. J. Transp. Eng. A-Syst. 143 (5), 04017009.

Luis, P.C., Roohollah, S., Georgios, V., John, B., et al., 2014. Monitoring strain gradients in adhesive composite joints by embedded fiber Bragg grating sensors. Compos. Struct. 112, 241-247.

Lyn, C., Yu, L., Wang, M.N., Xia, P.X., Sun, Y., 2020. Upper bound analysis of collapse failure of deep tunnel under karst cave considering seismic force. Soil Dyn. Earthq. Eng. 132, 106003.

Michalowski, R.L., Shi, L., 2003. Deformation patterns of reinforced foundation sand at failure. J. Geotech. Geoenviron. Eng. 129 (5), 439–449.

Moyo, P., Brownjohn, W.J.M., Suresh, R., Tjin, S.C., 2005. Development of fiber Bragg grating sensors for monitoring civil infrastructure. Eng. Struct. 27, 1828-1834.

Pei, H., Jing, J., Zhang, S., 2020. Experimental study on a new FBG-based and Terfenol-D inclinometer for slope displacement monitoring. Measurement 151, 107172.

Pei, H.F., Pang, C.J., B. Zhu, Z., Li, J., 2017. Magnetostrictive strain monitoring of cement-based magnetoelectric composites in a variable magnetic field by fiber Bragg grating. Constr. Build. Mater. 149, 904-910.

Qian, Q.H., Lin, P., 2016. Safety risk management of underground engineering in China: progress, challenges and strategies. J. Rock Mech. Geotech. 8 (4), 423-442.

Razouki, S.S., Schanz, T., 2011. One-dimensional consolidation under haversine repeated loading with rest period. Acta Geotech. 6, 13-20.

Sadeghi, J., Kian, A.R., Ghiasinejad, H., Moqaddam, M.F., Motevalli, S., 2020. Effectiveness of geogrid reinforcement in improvement of mechanical behavior of sand-contaminated ballast. Geotext. Geomembranes 48 (6), 768-779.

Song, H.B., Pei, H.F., Zhu, H.H., 2021. Monitoring of tunnel excavation based on the fiber Bragg grating sensing technology. Measurement 169, 108334.

Shankar, A., Suresha, S.N., 2011. Strength behaviour of geogrid reinforced shedi soil subgrade and aggregate system. Road Mater. Pavement 7 (3), 313-330.

Wang, M.C., Feng, Y.X., Jao, M., 1996. Stability of geosynthetic-reinforced soil above a cavity. Geotext. Geomembranes 14 (2), 95-109.

Xie, H., Liu, X.F., Zhang, H.J., Wang, E.Y., et al., 2022. Internal strain monitoring of coal samples based on fiber Bragg grating sensing. Measurement 187, 110355.

Xu, C., Liang, C., Shen, P., 2019. Experimental and theoretical studies on the ultimate bearing capacity of geogrid-reinforced sand. Geotext. Geomembranes 47 (3), 471-428.

Xu, J., He, J.P., Zhang, L., 2017. Collapse prediction of karst sinkhole via distributed Brillouin optical fiber sensor. Measurement 100, 68-71.

Xu, S.S., Lei, H., Li, C., Liu, H.Q., Lai, J.X., Liu, T., 2021. Model test on mechanical characteristics of shallow tunnel excavation failure in gully topography. Eng. Fail. Anal. 119, 104978.

Xu, Z.L., Luo, Y.B., Chen, J.X. Su, Z.M. Zhu, T.T., Yuan, J.P., 2021. Mechanical properties and reasonable proportioning of similar materials in physical model test of tunnel lining cracking. Constr. Build. Mater. 300, 123960.

Yetimoglu, T., Wu, J.T.H., Saglamer, A., 1994. Bearing capacity of rec-tangular footings on geogrid-reinforced sand. J. Geotech. Eng. 120 (12), 2083–2099.

Yoo, C., 2001. Laboratory investigation of bearing capacity behavior of strip footing on geogrid reinforced sand slope. Geotext. Geomembranes 19 (5), 279-298.

Yoshida, Y., Kashiwai, Y., 2002 Development of the monitoring system for slope deformations with fiber Bragg grating arrays. In: Proceedings of SPIE. pp. 296-303.

You, R.Z., Ren, L., Song, G.B., 2019. A novel fiber Bragg grating (FBG) soil strain sensor. Measurement 139, 85-91.

Zhao, Y.D., Shi, Y., Wu, F.H., Sun, R., Feng, H., 2021. Characterization of the sinkhole failure mechanism induced by concealed cave: A case study. Eng. Fail. Anal. 119, 105017.

Zhao, Y.J., Wang, F.G., Li, C.S., Cao Y.Q., Tian H.L., 2018. Study of the Corrosion Characteristics of Tunnel Fissures in a Karst Area in Southwest China. Geofluids 2018, 6234932.

Zheng, Y., Zhu, Z.W., Deng, Q.X., Xiao, F., 2019. Theoretical and experimental study on the fiber Bragg grating-based inclinometer for slope displacement monitoring. Opt. Fiber Technol. 49, 28-36.

Zheng, Y.H., He, S.Y., Yu, Y., Zheng, J.Y., Zhu, Y., Liu, T., 2021. Characteristics, challenges and countermeasures of giant karst cave: A case study of Yujingshan tunnel in high-speed railway. Tunn. Undergr. Space Technol. 114, 103988.